



2018

Global Ecosystems and Environment Observation
Analysis Research Cooperation

Temporal Dynamics and Spatial Distribution of
Global Carbon Source and Sink

National Remote Sensing Center of China,
Ministry of Science and Technology of the People's Republic of China



To support global change studies and international cooperation in Global Earth Observation System of Systems (GEOSS), the National Remote Sensing Center of China (NRSCC), Ministry of Science and Technology of the People's Republic of China has integrated a series of products from National Science and Technology Programmes to continuously produce and release annual reports from Global Ecosystems and Environment Observation Analysis Research Cooperation (GEOARC) since 2012.

As part of GEOARC–2018, we conducted a synthetic analysis of temporal and spatial distribution of global carbon sources and sinks, aiming to provide datasets and suggestions in support of international climate negotiations and the climate change mitigation and adaptation measures. We provide products such as the global atmospheric CO₂ column concentration and global solar induced chlorophyll fluorescence (SIF) retrieved from TanSat, global vegetation net primary production (NPP), key regional carbon sources and sinks using multi–source observational data and a carbon assimilation system. These data can be used to improve our understanding of global and regional carbon sources and sinks at higher spatiotemporal scales. The data and report are published at the website of National Integrated Earth Observation Data Sharing Platform (<http://www.chinageoss.org/geoarc/en/index.html>).

Foreword

The successful launch of China's carbon observing satellite (TanSat) is not only a positive action taken by China to combat global climate change, but also highlights the responsibility as one of large carbon emitting nations with growing economy. The records of atmospheric carbon dioxide (CO_2) column concentration and global vegetation productivity retrieved from the TanSat observational data can be used to improve our understanding of global and regional CO_2 sources and sinks at higher spatiotemporal scales. This can be accomplished by using an atmospheric model coupled to an assimilation system using the other multi-source data. Data products such as the global atmospheric CO_2 column concentration, global solar induced chlorophyll fluorescence (SIF), normalized difference vegetation index (NDVI), and gross primary productivity (GPP), are developed using data from Chinese TanSat, Japanese Greenhouse gases Observing SATellite (GOSAT), NASA's Orbiting Carbon Observatory 2 (OCO-2) and Moderate Resolution Imaging Spectroradiometer (MODIS), European Global Ozone Monitoring Experiment-2 (GOME-2), and other multi-source satellite remote sensing systems. A preliminary analysis was carried out and the global distribution of CO_2 sources and sinks and their dynamic changes in major regions of the world were obtained. The natural and anthropogenic drivers of the change due to fossil fuel combustion and the Earth's biosphere are discussed. Our aim is to provide global observations and analysis of carbon dynamics and data sets in support of the implementation of the climate conventions such as the Paris Agreement that supports climate change mitigation and adaptation measures such as China's carbon trading. It will guide China and the other countries along the path of green and low-carbon development.

1. Temporal and spatial variation characteristics of global atmospheric CO₂ concentrations

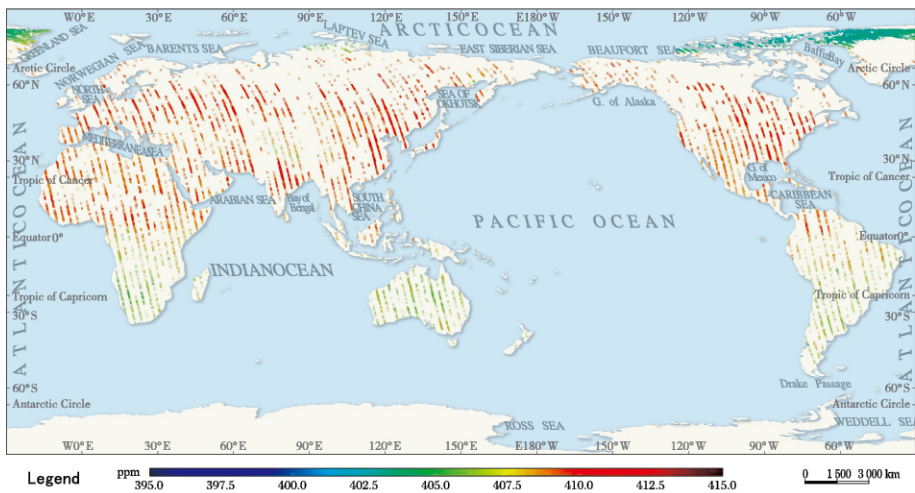
1.1 Spatial distribution of XCO₂

China successfully launched the global carbon dioxide observation satellite (TanSat) from Jiuquan Satellite Launch Center in December 2016. The radiance data collected by TanSat were analyzed by using China's own retrieval algorithm—Institute of Atmospheric Physics Carbon dioxide retrieval Algorithm for Satellite remote sensing (IAPCAS) (Yang et al., 2018) to retrieve the column-averaged atmospheric CO₂ dry air mole fraction (XCO₂) concentration distribution. Fig. 1-1 shows the global distribution of XCO₂ obtained from the TanSat retrieval in April and July 2017 (Yang et al., 2018; Liu et al., 2018).

In April 2017, the northern hemisphere had a high atmospheric CO₂ concentration while the southern hemisphere had a low atmospheric CO₂ concentration. The atmospheric CO₂ concentration reached about 410.0–415.0 ppm in high emission areas in the northern hemisphere. Areas showing high concentrations include North America, Western Europe, South Asia, and East Asia. High CO₂ concentrations in the northern hemisphere are caused by fossil fuel emissions and aided by weaker photosynthesis of vegetation in April. The CO₂ concentration in low-value zone in the southern hemisphere is between 395.0 and 400.0 ppm, with spatial variations in the

atmospheric CO₂ concentration in the northern and southern hemispheres of ~ 20.0 ppm.

In July 2017, vegetation growth in the northern hemisphere led to stronger photosynthetic CO₂ uptake than in April. Because of the large oceanic extent in the southern hemisphere and low seasonal variation of carbon absorption, the concentration difference between the northern and southern hemispheres is not obvious. The CO₂ concentration in the northern hemisphere from spring to summer shows a decreasing trend, which indicates the characteristics of the "carbon sequestration" of terrestrial ecosystems with seasonal changes.



(a) April 2017

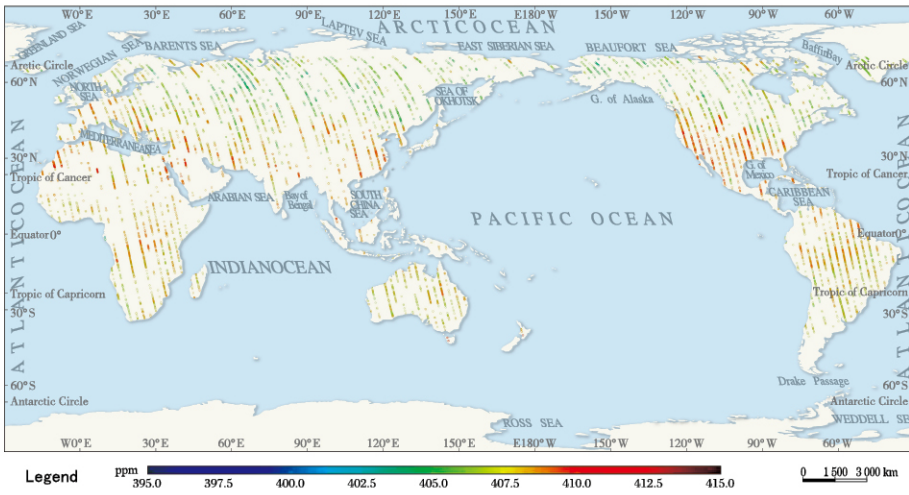


Fig. 1–1 Global distribution of atmospheric CO_2 from TanSat in (a) April and (b) July 2017. The color scale indicates the column-averaged atmospheric CO_2 dry-air mole fraction (XCO_2)

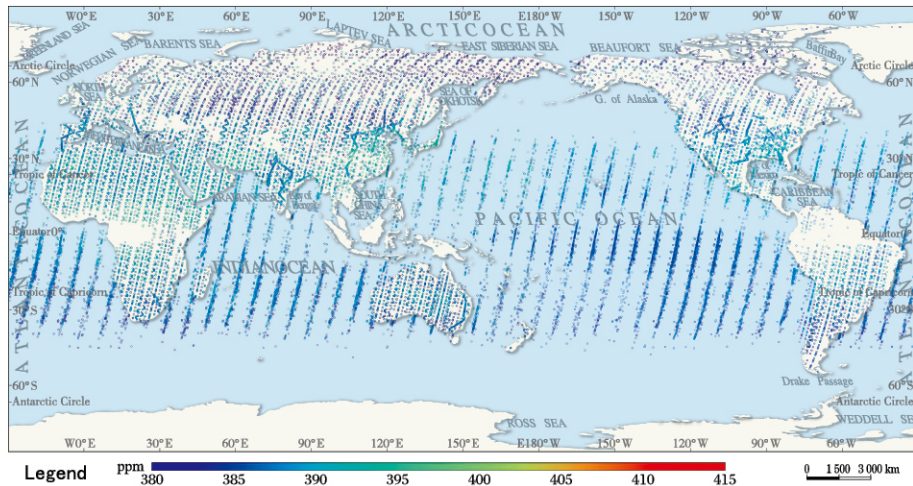
1.2 Interannual variation of XCO_2

The results of the carbon monitoring satellite (Fig. 1–2) show that the global average annual atmospheric CO_2 concentration grew linearly from 2010 to 2017, with an average annual growth rate of 2.2 ppm/yr and an average annual value of 402.8 ppm in 2017. During this period, the global atmospheric CO_2 concentration showed a seasonal fluctuation, which peaks in spring every year and falls to the minimum in summer. The difference between maximum and minimum values is about 2.9–7.1 ppm.

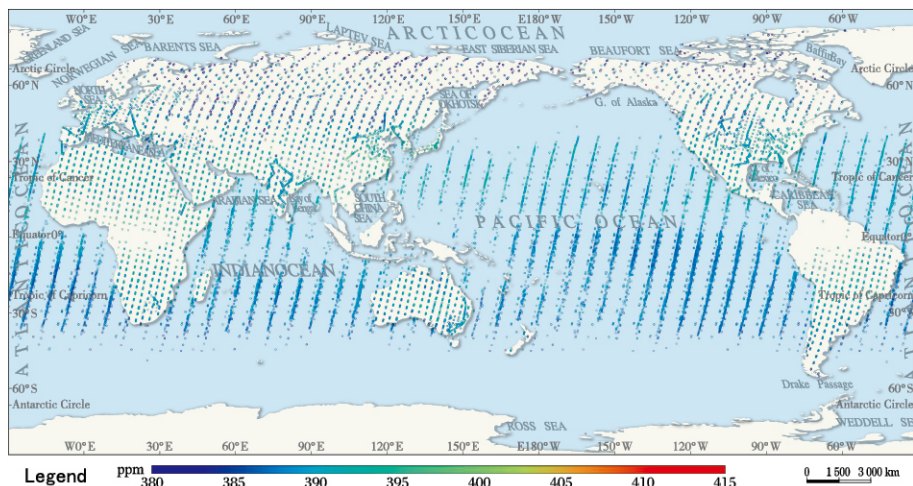


Fig. 1–2 Global monthly and annual CO_2 emissions from 2010–2017 derived from GOSAT data v02.72

The results from the carbon monitoring satellite show that the annual average of global atmospheric CO_2 concentrations has continued to increase (Fig. 1–3). In 2010, the annual average global atmospheric CO_2 concentration was 387.4 ppm, and 83% area was below 390.0 ppm (Fig. 1–3a). In 2013, global atmospheric CO_2 concentrations averaged 393.4 ppm, and 90% of satellite remote sensing observations were larger than 390.0 ppm (Fig. 1–3d). In 2016, satellite monitoring of the global average atmospheric CO_2 concentration reached 400.0 ppm for the first time, and 59% of the satellite remote sensing observations were greater than 400.0 ppm (Fig. 1–3g). In 2017, the global average atmospheric CO_2 concentration reached 402.9 ppm, and 83.7% of the satellite remote sensing observations were greater than 400.0 ppm (Fig. 1–3h).

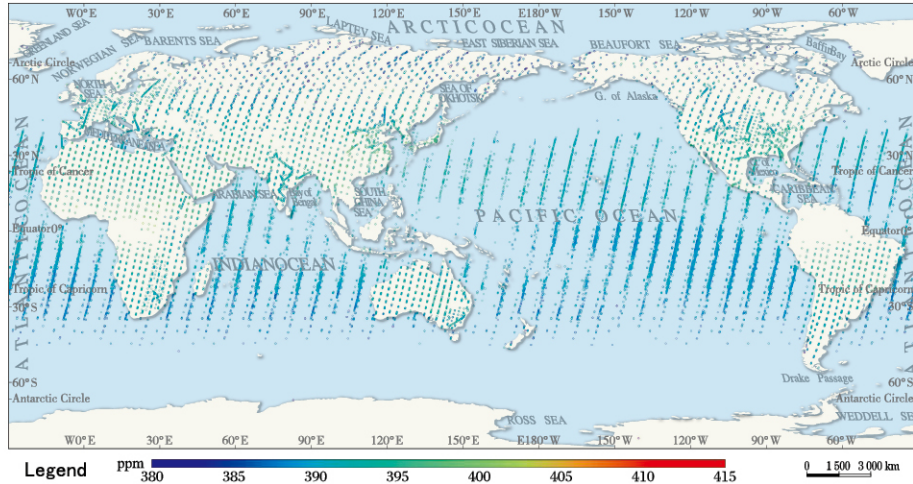


(a) 2010

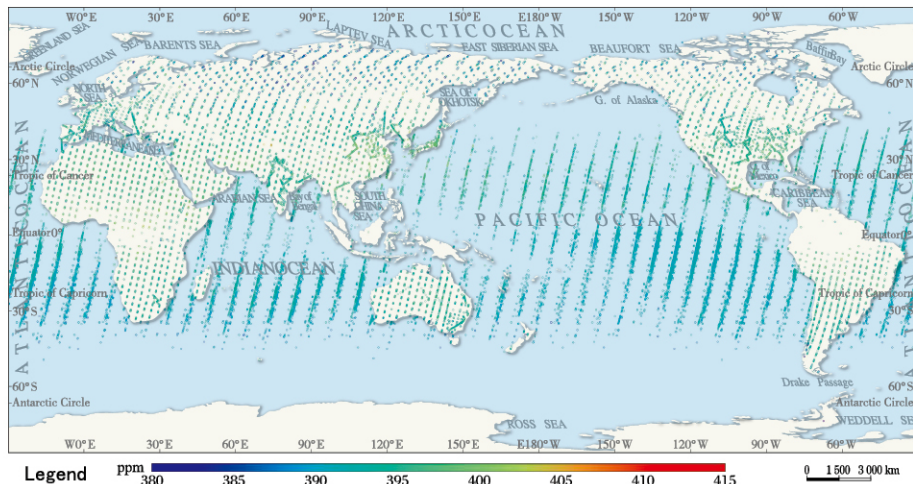


(b) 2011

Temporal Dynamics and Spatial Distribution of Global Carbon Source and Sink



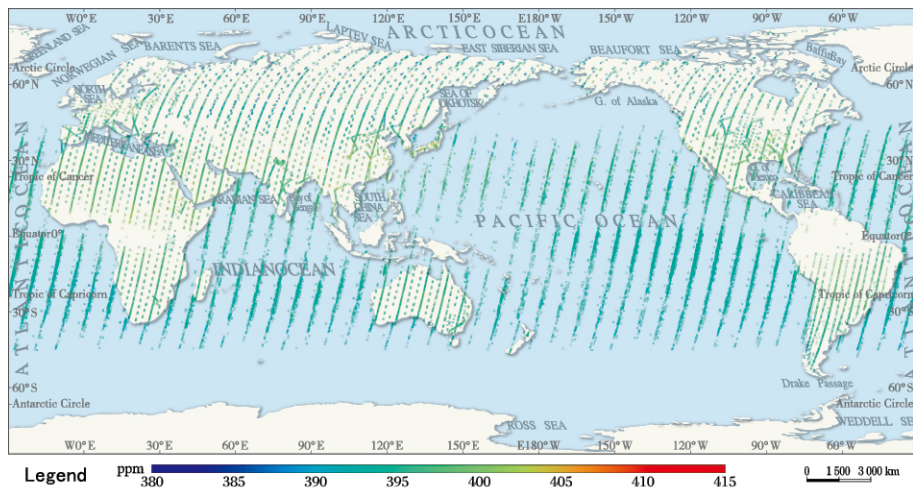
(c) 2012



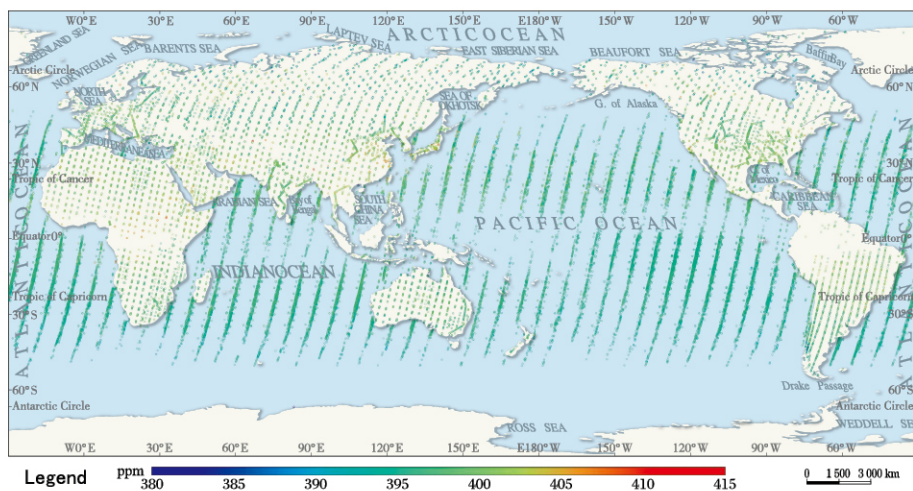
(d) 2013

2018

Global Ecosystems and Environment Observation Analysis Research Cooperation



(e) 2014



(f) 2015

Temporal Dynamics and Spatial Distribution of Global Carbon Source and Sink

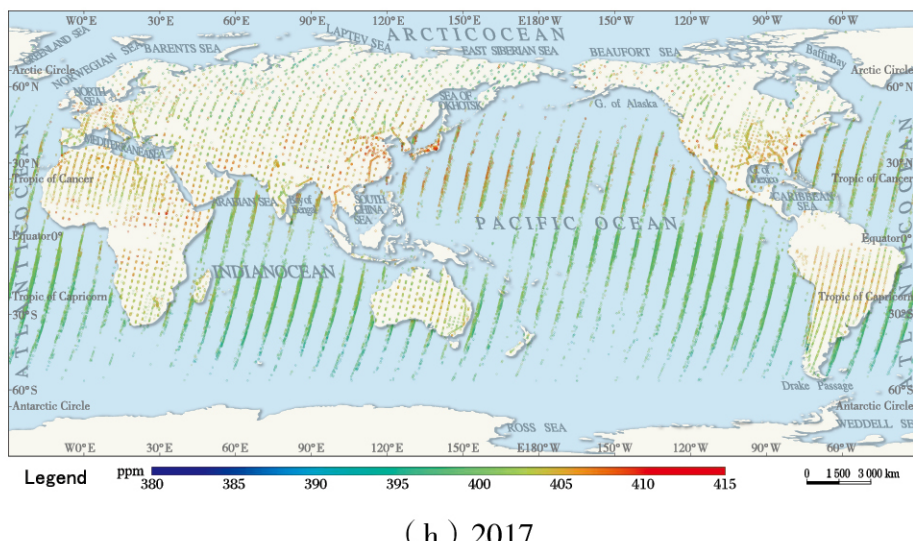
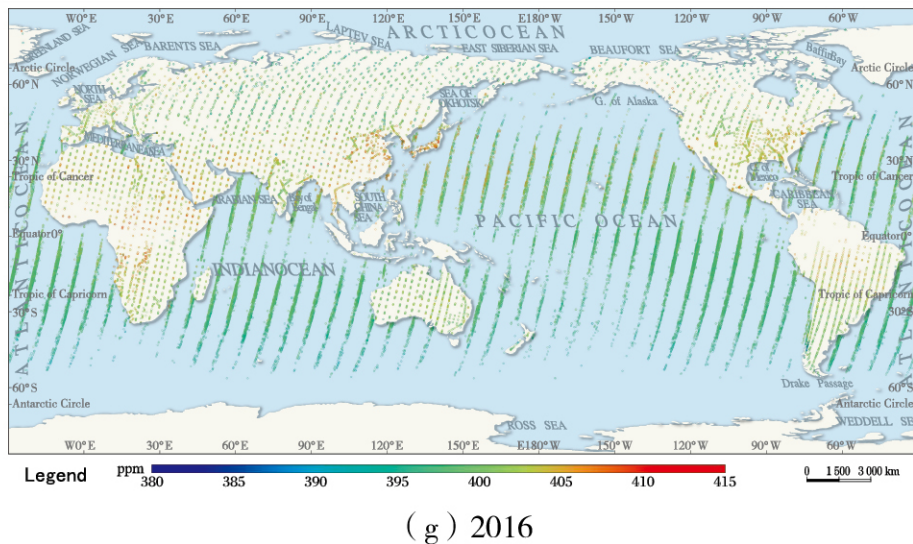


Fig. 1–3 Global atmospheric XCO_2 concentration from 2010–2017 derived from GOSAT. Note that the color bar of the eight subplots is the same, and the color changes from blue to red over the years, indicating that the CO_2 concentration is increasing

1.3 Seasonal variation of XCO₂

By analyzing the spatial distribution of global atmospheric CO₂ concentration in different seasons (Fig. 1–4), it is apparent that the period of high CO₂ concentration in the northern hemisphere is mainly concentrated in winter and spring. The average winter CO₂ concentration is 404.5 ppm, which is a result of the burning fossil fuels for heating, industry, power generation, traffic ,etc.,and the lack of carbon uptake through plant photosynthesis. In the northern hemisphere, the atmospheric CO₂ concentration was the highest in the spring, with an average of 405.9 ppm. The cumulative effect of atmospheric CO₂ during the winter and spring seasons caused the atmospheric CO₂ concentration in the northern hemisphere to peak in spring. In the northern hemisphere, the atmospheric CO₂ concentration is the lowest in summer, with an average of 401.9 ppm, mainly due to the enhanced ability of summer plant photosynthesis to absorb atmospheric CO₂. The average global atmospheric CO₂ concentration in the fall is 402.5 ppm.

The southern hemisphere is opposite to the seasonal changes in the northern hemisphere. In the northern hemisphere winter and spring (December 2016–May 2017), the atmospheric CO₂ concentration in the southern hemisphere is relatively low, mostly between 390.0–405.0 ppm. In the summer and autumn of the northern hemisphere (June–November 2017), the atmospheric CO₂ concentration in the southern hemisphere increased slightly. The atmospheric CO₂ concentration value in the southern hemisphere is relatively small, which is comparable to the northern hemisphere summer (June–August).

In general, the atmospheric CO₂ concentration in the northern hemisphere is highest during winter and spring, followed by autumn and summer. The atmospheric CO₂ concentration in the southern hemisphere changes little, and is maintained at a low level of 390.0–405.0 ppm.

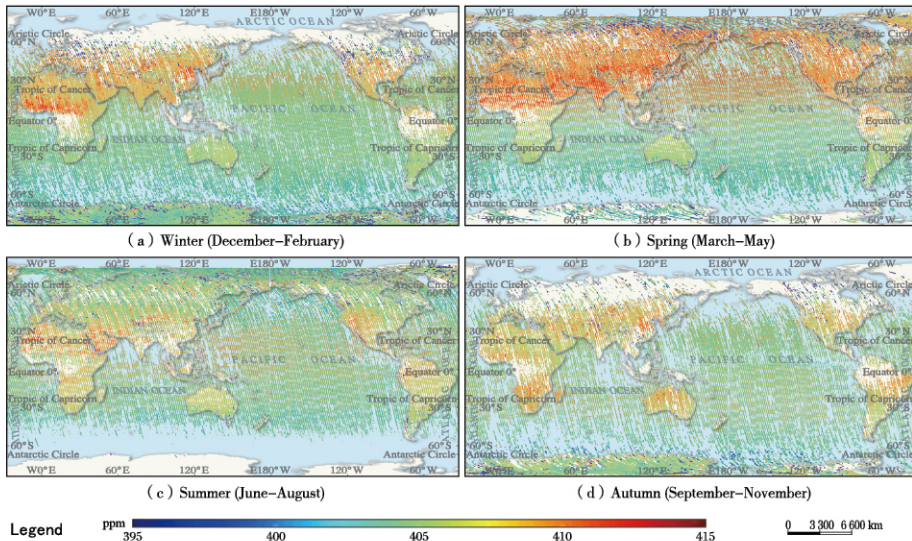


Fig. 1–4 2017 global XCO₂ distribution based on OCO-2 satellite observations. The four figures are (a) winter, (b) spring, (c) summer, (d) autumn, and the CO₂ concentration was highest for the northern hemisphere in spring

2. The distribution of global carbon sources and sinks and the causes of its dynamics

2.1 Fossil fuel CO₂ emissions

According to the global high-resolution emission data of 2016 (Fig. 2-1), there are four high-value emission centers in the world with emission intensity of 100–600 gC/m²/yr, which are located in the Central United States, Eastern United States, Central Europe, Western Europe, Eastern Asia, and industrial region of South Asia. Africa, Oceania, Central South America, Northern North America, and northern Eurasia are low-value discharge zones with emission intensity below 5 g C/m²/yr.

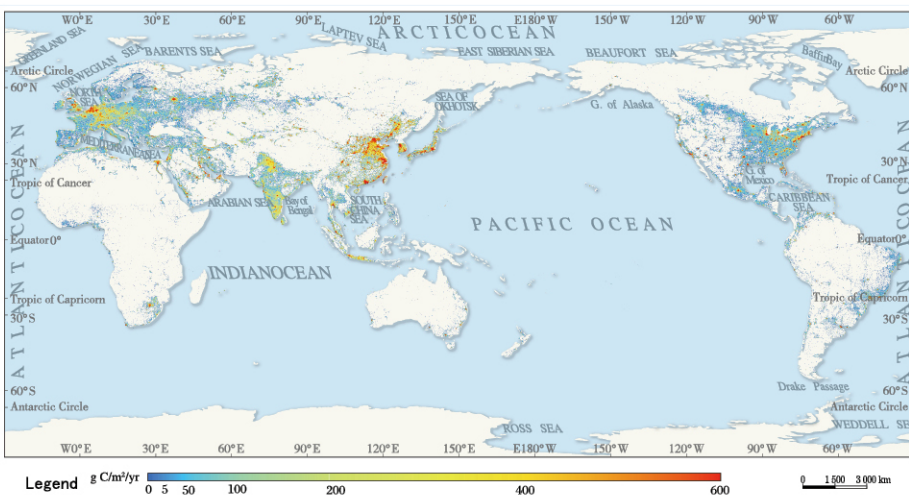


Fig. 2-1 CO₂ emissions from global fossil fuel combustion and cement production in 2016 with a spatial resolution of 10 km derived from ODIAC (Oda et al., 2018, <http://db.cger.nies.go.jp/dataset/ODIAC/>)

From 1960–2016, the global fossil fuel and industrial CO₂ emissions increased yearly, with CO₂ emissions of about 2.5 Pg C/yr in 1960 and 9.9 Pg C/yr in 2016, 4 times the emissions of 1960 (Fig. 2–2) (Boden et al., 2017; Le Quéré et al., 2018). In the past four decades, the CO₂ emission rate has varied. Around 1980, the CO₂ emissions decreased slightly and the emission rate was negative. From 2002 to 2008, the CO₂ emission rate was high. During this period, global industry developed rapidly and large quantities of fossil fuels were burned. The slowdown in emissions since 2011 is mainly due to industrial and energy restructuring in developed countries (Le Quéré et al., 2018).

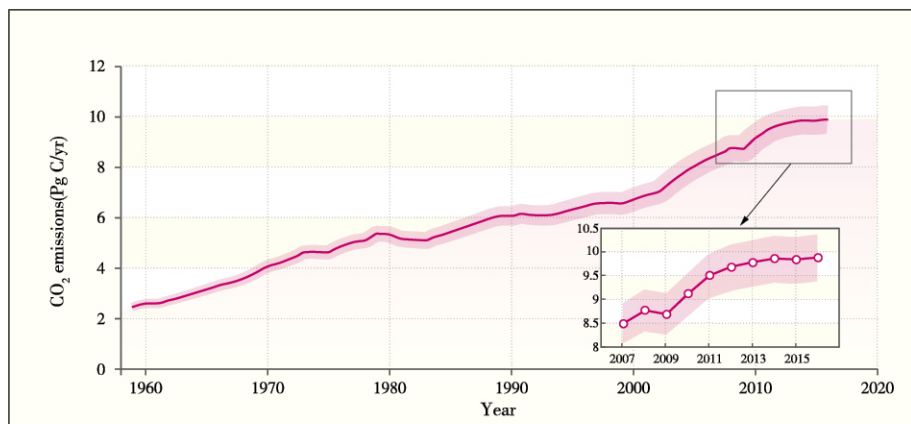
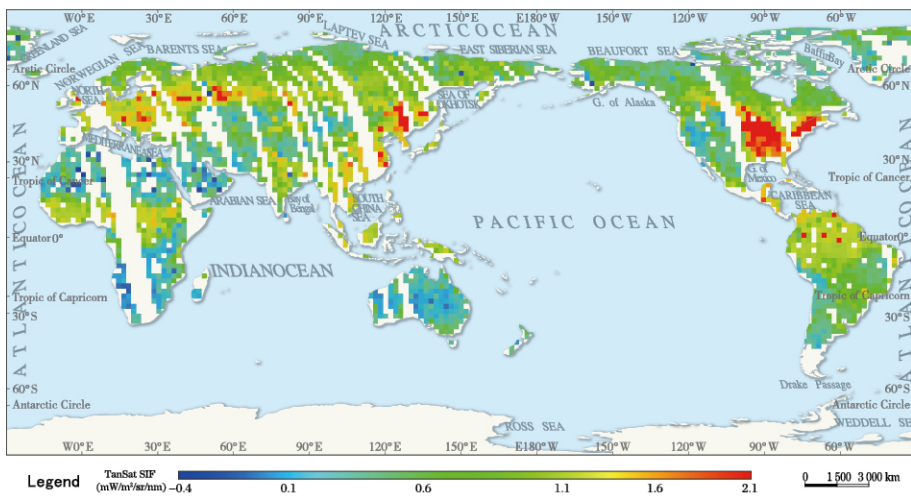


Fig. 2–2 Global fossil fuel and industrial CO₂ emissions from 1960–2016. The inset map shows CO₂ emissions from 2007–2016, which levels off after 2013, data derived from (Le Quéré et al., 2018), 2015 and 2016 estimates are based on energy statistics published by BP (<https://www.bp.com/content/dam/bp/en/corporate/pdf/energy-economics/statistical-review-2017/bp-statistical-review-of-world-energy-2017-full-report.pdf>)

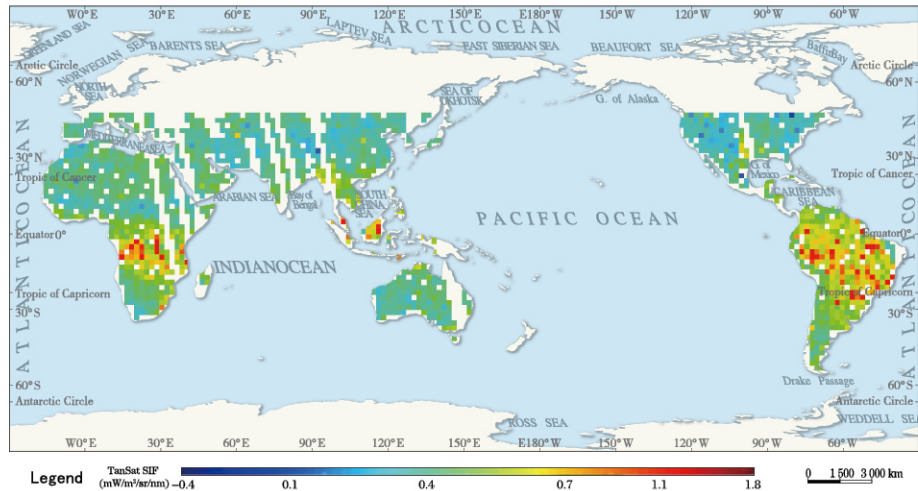
2.2 Global terrestrial carbon budgets

2.2.1 Global chlorophyll fluorescence and spatial and temporal patterns of GPP

Plants produce organic matter by fixing atmospheric CO₂ through photosynthesis, which is the main process regulating CO₂ exchange between the land and atmosphere. Plants only fluoresce when photosynthesis occurs, and chlorophyll fluorescence directly reflects the ability of plants to absorb carbon. Using the Chinese carbon satellite (TanSat) to obtain global chlorophyll fluorescence distribution, the results clearly show the vigorous productivity of vegetation in July 2017 in the North American agricultural regions, the European Plains, East Asian agricultural planting regions, Southeast Asia, the Amazon rainforest and other regions (Fig. 2–3)(Du et al., 2018). The results also captured the dynamic changes of summer and winter vegetation productivity and carbon sink capacity in the northern and southern hemispheres.



(a) July 2017



(b) December 2017

Fig. 2–3 TanSat's first global solar induced chlorophyll fluorescence product in (a) July and (b) December 2017

Total gross primary productivity (GPP) refers to the total amount of organic carbon fixed by plants through photosynthesis per unit time and is the world's largest carbon flux (about 120 billion tons per year). The global spatial and temporal distribution pattern of GPP is the key to the balance of terrestrial carbon balance, which can affect the distribution of terrestrial vegetation carbon sinks.

The spatial distribution of global GPP in 2017 was estimated based on solar-induced chlorophyll fluorescence information from satellite observations and observations from the Global Flux Observing Network (FLUXNET). The results show that the global GPP average value was 651.0 g C/m²/yr in 2017 (Fig. 2–4). Areas with high GPP appear in the central and southern Amazon rainforests of central America, the central African

rainforests, the Southeast Asian and European plains. The GPP values are lower in the high latitudes of northern North America, the deserts of northern Africa, northwestern Asia and the southwestern region of Oceania.

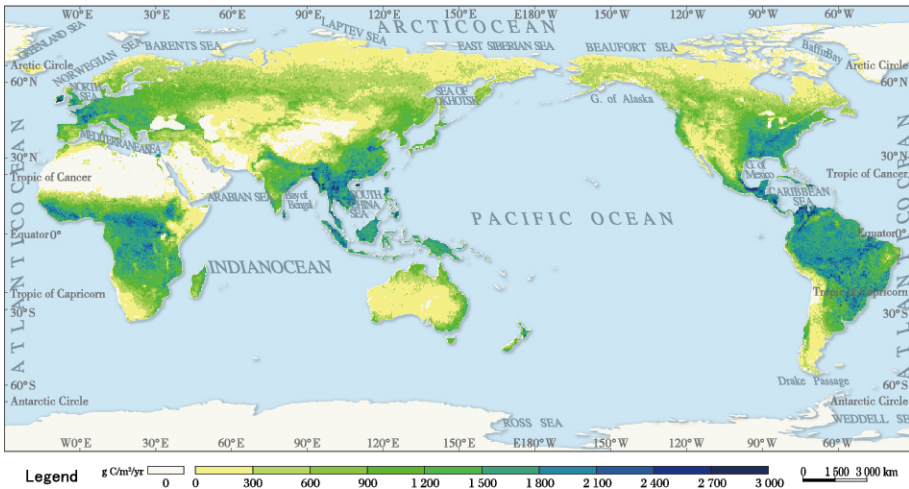


Fig. 2-4 Spatial distribution of the global GPP in 2017, which was calculated using GOME-2 SIF and FLUXNET data (<http://fluxnet.fluxdata.org/data/fluxnet2015-dataset/>)

2.2.2 Global terrestrial vegetation carbon sinks

Global terrestrial carbon sinks are derived from the absorption and storage of atmospheric CO₂ by ecosystems such as forests, grasslands, farmland, and shrubs. Based on the TRENDY multi-model simulation results of terrestrial vegetation and atmospheric interaction, the global terrestrial carbon sinks reached 3.0 ± 0.8 Pg/yr during the period of 2007 through 2016, showing a slow increasing trend (Le Quéré et al., 2018). The study found that: (1) Forests are the largest carbon stocks in terrestrial ecosystems. Tropical forests are mainly distributed in South America, Africa and Southeast Asia, and their forest carbon sinks account for about 50%

of global forest carbon sinks. Temperate forests are mainly distributed in the southern part of North America, southern Europe, China, Japan, South Korea and Australia, and their forest carbon sinks account for about 29% of global forest carbon sinks. Cold temperate forests are mainly distributed in Canada, northern Europe and Russia, and their forest carbon sinks account for about 21% of global forest carbon sinks. Global forests play an important role in reducing atmospheric greenhouse gas concentrations and slowing global warming. (2) Unlike forests, most of the carbon in grassland is stored in the soil. The grassland soil carbon pool accounts for more than 10% of the global soil carbon pool, and it plays an important role in the global terrestrial ecosystem carbon cycle. (3) The carbon fixed in the farmland ecosystem will return to the atmosphere in a short period of time, so on the interdecadal scale (>10 years), the farmland ecosystem has less impact on the global carbon cycle. For each growing season, the size of the farmland ecosystem carbon sink will be affected by various farmland management measures.

2.3 Distribution of global carbon sources and sinks based on a model–data assimilation product

The distribution pattern from the carbon assimilation system (LETKF–Carbon) of global carbon sources and sinks averaged over the period of 2012–2016 is shown in Fig. 2–5. Due to the spatial heterogeneity of ecosystem types and anthropogenic carbon sources, the spatial differences in terrestrial carbon sinks are large. In the Asia, North America and Europe, anthropogenic emissions are high; whereas in Oceania, Africa and South America, anthropogenic emissions are weak. The terrestrial carbon sinks in Asia, North America and Europe are strong, and the terrestrial carbon sinks

in Oceania, Africa and South America are weak. The results of the carbon assimilation system optimization show that the Asia and North America are strong carbon sources, and Oceania, Africa are weak carbon sources.

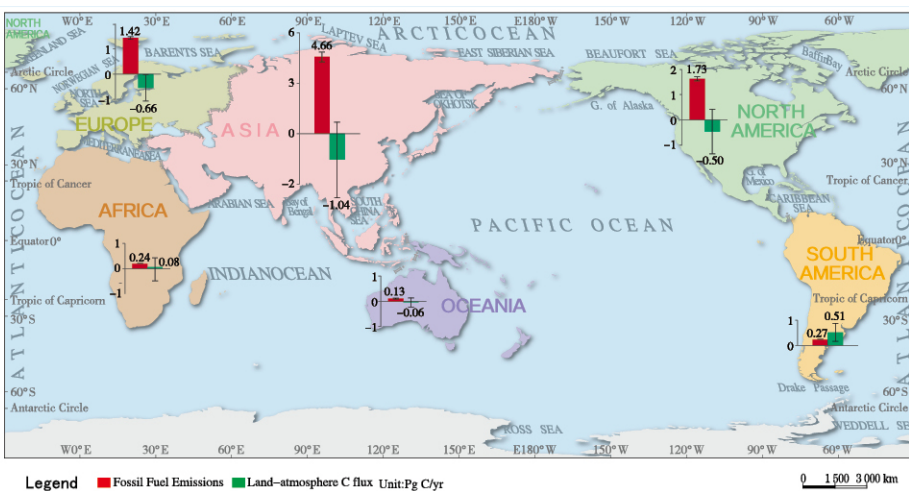


Fig. 2–5 Global carbon sources and sinks from 2012–2016 based on the LETKF carbon assimilation system. The bar graph represents the total carbon fluxes of each region (the left bar graph represents the prior anthropogenic emissions; the right bar graph represents the optimized ecosystem land-to-atmosphere carbon fluxes)

2.4 The impact of the agricultural Green Revolution on carbon sinks

The intensive farming methods of the agricultural Green Revolution are rapidly changing the distribution of global carbon. From 1961 to 2010, the main crop acreage increased by 20%, while the total crop production increased by a factor of three (Fig. 2–6). The Green Revolution featured by management practices—using high-yield varieties, expanding irrigated areas and increasing the use of fertilizers and pesticides—not only increased

crop yields, biomass and thus carbon sinks, but also extended crop growth period and residue decay time. These practices also increased the seasonal variation of atmospheric CO₂ concentrations, and had an impact on carbon sources and sinks.

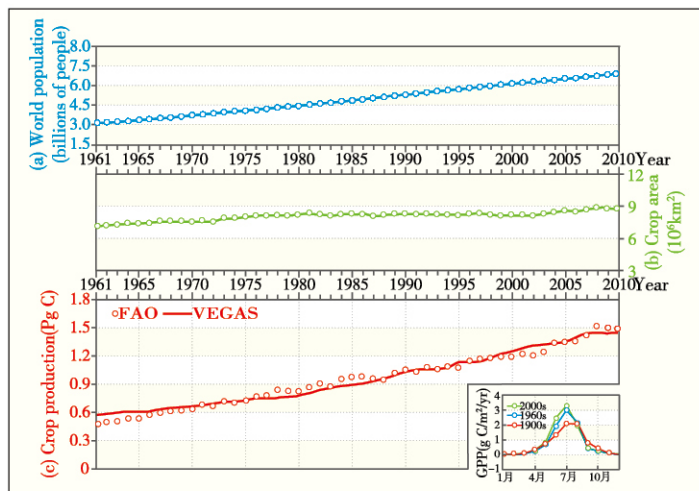


Fig. 2-6 Changing world population, land area of major crops, annual crop production and changes in crop GPP seasonal cycle. Crop production tripled (a) to support 2.5 times more people (b) on only 20% more cropland area (c), enabled by the agricultural Green Revolution. Plotted in (c) is the VEGAS model simulated crop production, compared to the estimate from FAO statistics. The inset in (c) shows modeled GPP for the periods 1901–1910, 1961–1970 and 2001–2010 for a location in the US Midwest agricultural belt (98°W–40° N) that was initially naturally vegetated and later converted to cropland. The change in seasonal characteristics from these transitions may have contributed to the change in atmospheric CO₂ seasonal amplitude

In the agricultural regions of Northeast China, the North China Plain, Central Europe, Western Europe, and the Great Plains of the United States, the highest NPP increase is 0.12–0.18 g C/m²/yr. These areas are also carbon sinks

in late summer and early autumn. The high production areas are consistent with the TanSat SIF products, and are also consistent with the spatial distribution of global atmospheric CO₂ concentration and carbon assimilation analysis. The VEGAS model estimates that global crop yields are similar to the FAO statistics, further indicating that the agricultural Green Revolution plays an important role in the global carbon cycle and is one of the important reasons for the increase of the seasonal amplitude of CO₂.

2.5 Global carbon cycle response to El Niño

The El Niño–Southern Oscillation (ENSO) is the main internal inter annual variability of the climate system, which causes temperature and precipitation anomalies in different regions of the world through teleconnections. The interannual variability of the atmospheric CO₂ concentration is significantly correlated with ENSO, that is, in El Niño years, the interannual growth rate of atmospheric CO₂ is abnormally increased, while the opposite occurs during La Niña years (Fig. 2–7). The interannual growth rate of atmospheric CO₂ concentration mainly comes from terrestrial ecosystems. Anomalies in temperature and precipitation caused by ENSO are the main climate driving factors leading to the interannual anomalies of terrestrial carbon cycle.

The most recent El Niño event occurred in 2015/16, causing an increase in global terrestrial precipitation anomaly of 0.02 mm/day and an increase in near-surface temperature anomaly of 0.31°C (average from July 2015 to October 2016). Results from the dynamic global vegetation model (VEGAS; Zeng et al., 2005) simulations show an abnormal release of global land–atmosphere carbon flux of 0.73 Pg C/yr during the 2015/16 El Niño event, which is close to the

0.82 Pg C/yr obtained by CarbonTracker inversion (Peters et al., 2007). The anomalous absorption seen in the northern hemisphere is 0.52 Pg C/yr, while in the tropics and southern hemisphere, the anomalous release is 1.12 Pg C/yr and 0.14 Pg C/yr, respectively (Wang et al., 2018).

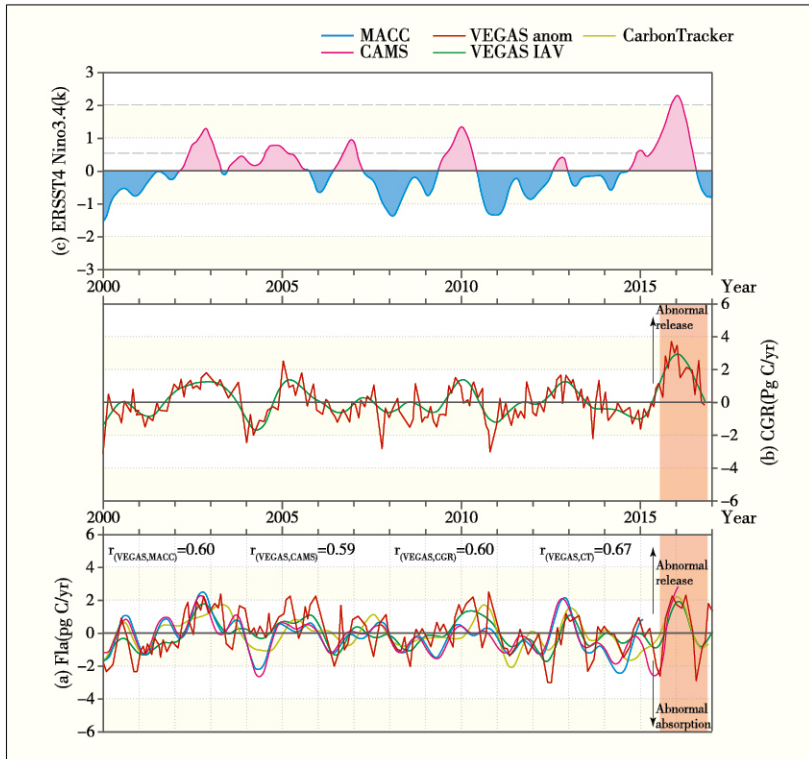


Fig. 2–7 Interannual variability of ENSO and carbon cycle. (a) ERSST4 Nino3.4 index; (b) Mauna Loa atmospheric CO₂ growth rate. Red represents the original monthly data and green line is 1–10 year bandpass filtered; (c) Comparison of global total land–atmosphere carbon flux anomalies from the VEGAS model and two atmospheric inversions CAMS and MACC

3. Analysis of carbon sources and sinks in key areas

3.1 Continental regions

Starting in 2000, Asia's fossil fuel CO₂ emissions were the highest ever and increased yearly through 2015, with an average annual CO₂ emission of 3.75 Pg C (Fig. 3–1). Other continents saw much smaller changes in CO₂ emissions, with the average CO₂ emissions of Europe, North America, South America, Africa, Oceania being 1.50, 1.72, 0.30, 0.26, and 0.11 Pg C, respectively.

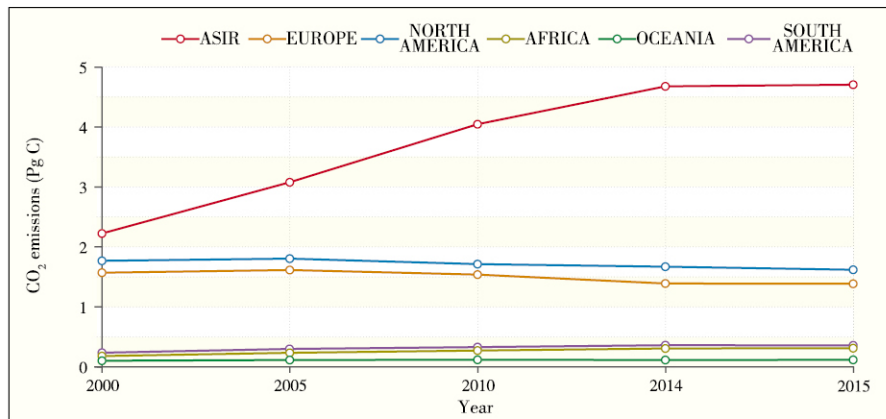


Fig. 3–1 Continental scale fossil fuel CO₂ emissions from 2000–2015, data based on BP (<https://www.bp.com/content/dam/bp/en/corporate/excel/energy-economics/statistical-review/bp-stats-review-2018-all-data.xlsx>) and IEA (CO₂ emissions from fuel combustion highlights (2017 edition))

Note: The CO₂ emissions data based on BP reflect only those through consumption of oil, gas and coal for combustion related activities.

From 2012 through 2016, Asia's carbon sink intensity is higher than that of other regions, showing strong carbon sinks with an average carbon

sink intensity of 1.04 Pg C. During the same period, the average carbon sink strengths of Europe, North America, Oceania were 0.66, 0.50, 0.06 Pg C, respectively. In addition, there are significant interannual differences in carbon sinks across continents, mainly due to precipitation and temperature anomalies caused by climate variability such as ENSO (Fig. 3–2).

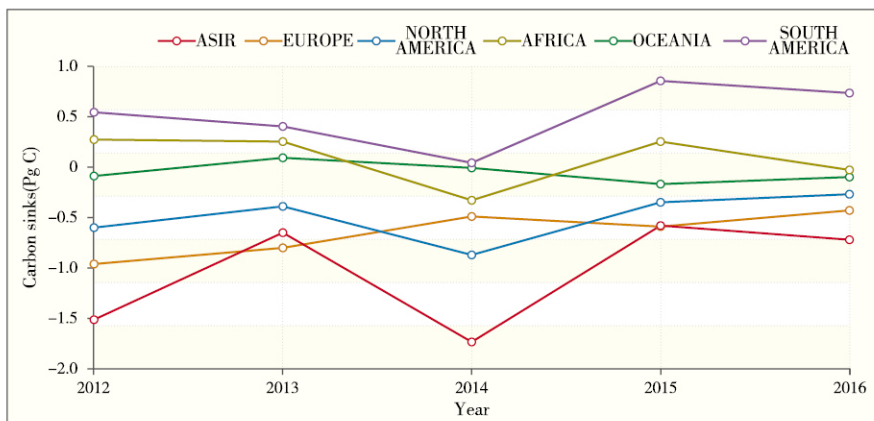


Fig. 3–2 Changes in carbon sinks/sources in terrestrial ecosystems for continents from 2012–2016 based on LETKF carbon assimilation system

3.2 China

3.2.1 Carbon emissions

From 2010 through 2017, China's fossil fuel CO₂ emissions were generally on the rise. During 2010–2013, CO₂ emissions increased rapidly, from 2.21 Pg C in 2010 to 2.52 Pg C in 2013; a slight downward trend in 2013–2016; and a slight increase in 2017, reaching 2.52 Pg C (Fig. 3–3).

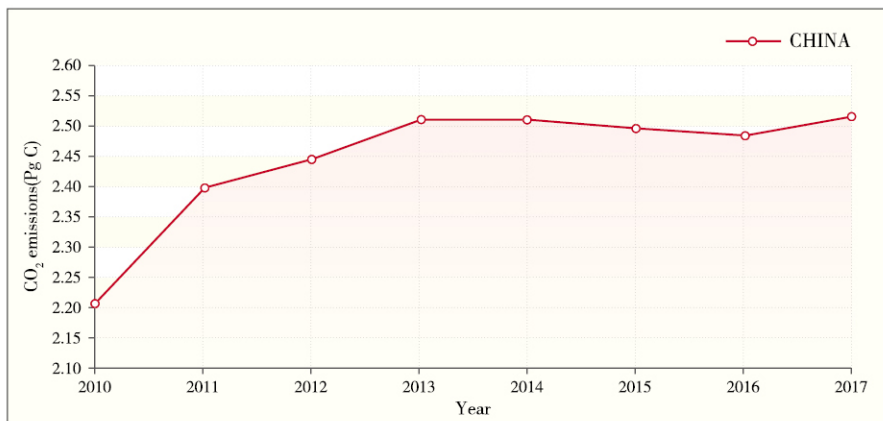


Fig. 3–3 China's fossil fuel CO₂ emissions from 2010–2017. And the emission peaked at 2013, data based on BP (<https://www.bp.com/content/dam/bp/en/corporate/excel/energy-economics/statistical-review/bp-stats-review-2018-all-data.xlsx>)

Note: The CO₂ emissions data based on BP reflect only those through consumption of oil, gas and coal for combustion related activities.

3.2.2 Industrial adjustment contributions to carbon emission reduction

Compared with thermal power, carbon emissions reduction from hydroelectricity, wind, solar, and nuclear generation has increased every year from 2010 through 2017 (Fig. 3–4). In 2017, the total carbon emission reduction of hydroelectricity, wind, solar and nuclear was 425.48 Tg C (Fang et al, 2012; Liu, 2013; Qin, 2011; Zhao, 2010; Ma, 2002; Jang, 2015; Shi et al, 2013; Xia, 2010). The National Climate Change Plan (2014–2020) issued by the National Development and Reform Commission of the People's Republic of China predicts that by 2020, China's hydroelectricity, wind, solar, and nuclear installed capacity will reach 3.5, 2, 1, 0.58 million

kilowatts, respectively. Then, in 2020, the total carbon emission reduction of hydroelectricity, wind, solar and nuclear is about 479.71 Tg C.

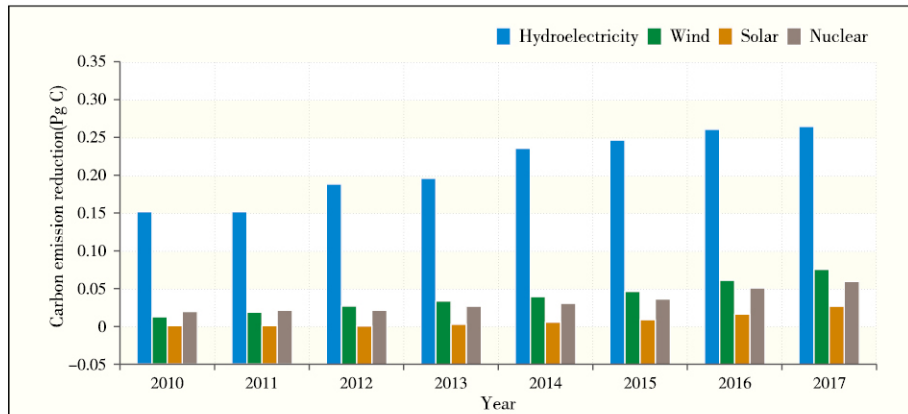


Fig. 3–4 Carbon emission reduction introduced by hydroelectricity, wind, solar and nuclear use from 2010–2017. Power generation data based on China Electricity Council (<http://www.cec.org.cn/guihuayutongji/tongjixinxi/>)

3.2.3 Terrestrial ecosystem carbon sinks

According to the statistics of a series of articles published in the Proceedings of the US National Academy of Sciences (PNAS) in 2018, the total carbon stock of China's terrestrial ecosystem is 89.27 ± 1.05 Pg C. The total carbon pool of forests, grasslands, shrubs, and farmland is 79.24 ± 2.42 Pg C, of which forest accounts for 38.9%, grassland 32.1%, shrub forest 8.4%, and farmland 20.6%. In 2001–2010, the average annual carbon sequestration of China's terrestrial ecosystems was 201.1 Tg C, equivalent to offsetting 14.1% of China's fossil fuel combustion CO₂ emissions during the same period. Forest ecosystems contributed the most to carbon sequestration (163.4 Tg C, 80%), followed by farmland (24.0 Tg C, 12%), and shrubs (17.3 Tg C, 8%) (Fig. 3–5). In the next 10 to 20 years, the forest ecosystem will

have a carbon sequestration potential of 1.9–3.4 Pg C due to the natural growth of the forest.

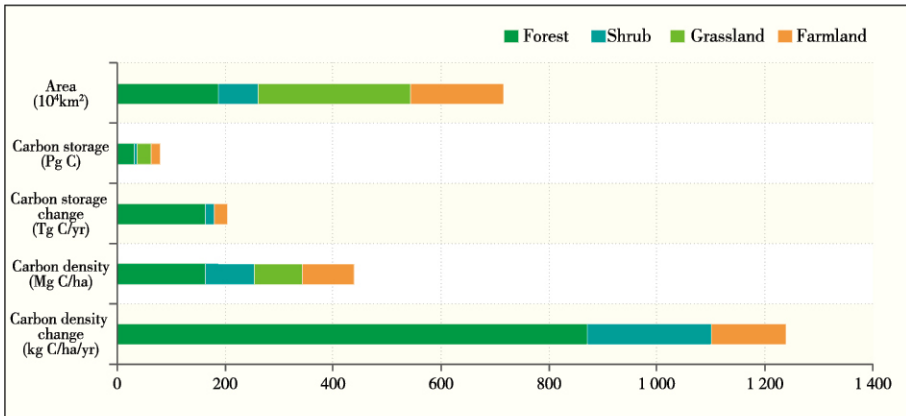


Fig. 3–5 Carbon sequestration in China's major terrestrial ecosystems in forest (dark green bars), shrubs (blue bars), grasslands (light green bars) and cropland (orange bars) (Tang et al., 2018)

In addition, in the past 20 years, China has implemented several major ecological projects such as natural forest protection, shelter forests, and Grain for Green Project (GGP), which has greatly reduced the effect of climate change caused by CO_2 emissions. From 2001 to 2010, the implementation of six major ecological projects in China increased the carbon sequestration by 56%, with the annual carbon sink being 74 Tg C/yr (the total carbon sink in the entire ecological engineering area was 132 Tg C/yr), equivalent to 50–70% of China's main terrestrial ecosystem carbon sinks, or 9.4% of China's fossil fuel combustion carbon emissions.

From 1950 to 2010, the net carbon uptake of new afforestation vegetation in China was 1.69 Pg C, and by 2050 the net fixed carbon amount would reach 3.17 Pg C. Nationally, the average soil organic carbon stock in topsoil (0–20 cm) increased from 28.6 t C/ha in 1980 to 32.9 t C/ha in 2011,

with a net increase of 140 kg C/ha/yr.

The vegetation indices based on remote sensing data (NDVI) has a good positive correlation with vegetation productivity and can reflect the change of ecosystem carbon sinks (Fang et al., 2007). Based on the analysis of China's NDVI dataset in 2010–2017, the annual average NDVI showed a significant increase from 2010 to 2017, which showed the improvement of the ecosystem function (Fig. 3–6). In terms of spatial distribution, the area for significantly improvement of NDVI accounted for 27.3% of the national land area, mainly in humid and semi-humid areas such as South China, North China, and Northeast China; the percent of the significant reduction area was only 0.9%. This trend shows that the vegetation condition improved and the ecosystem carbon sink capacity had gradually increased for the implementation of ecological engineering in China (Fig. 3–7).

All in all, China's terrestrial ecosystems are a significant carbon sink, and both climate change and human management contribute to this carbon sink.

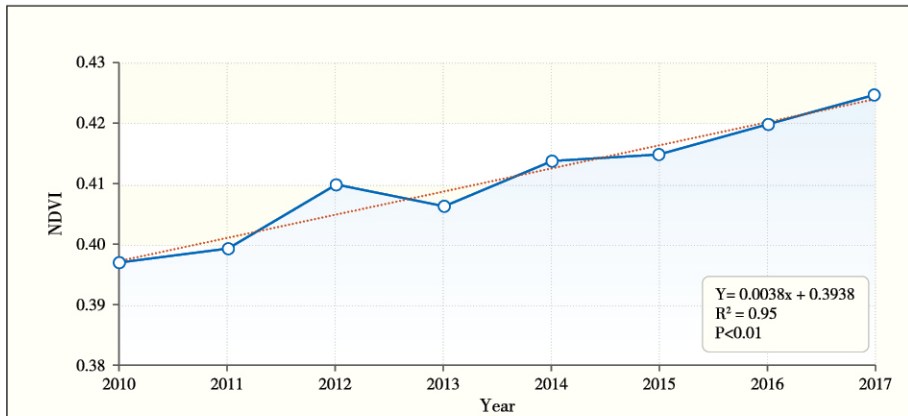


Fig. 3–6 Interannual variations of NDVI in China from 2010 to 2017. The blue hollow dots indicate the annual average of NDVI, and the red line indicates the NDVI trend line from 2010–2017

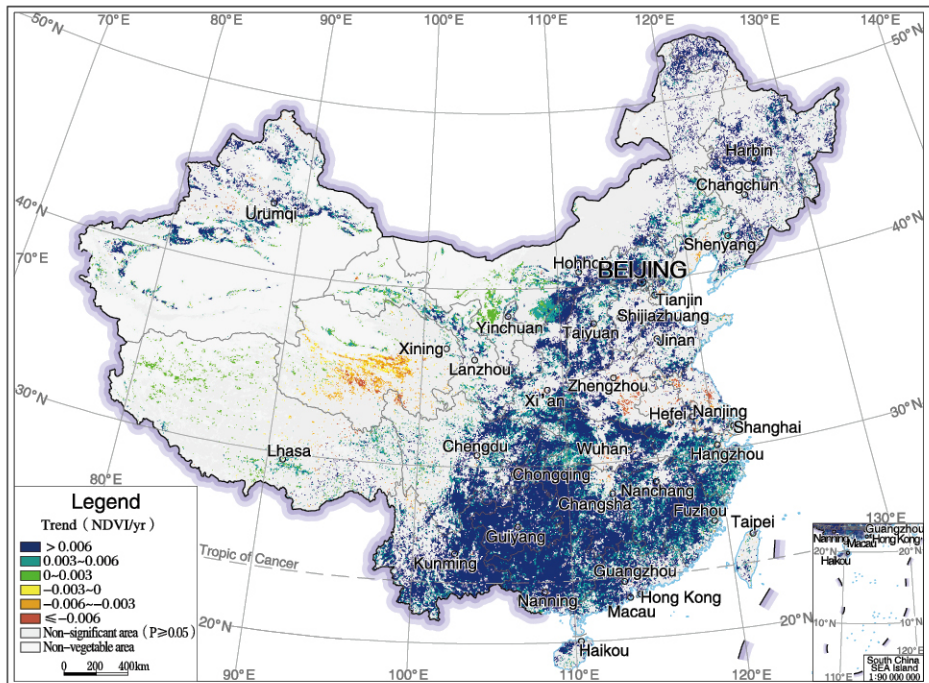


Fig. 3–7 Annual mean NDVI trend and spatial significance test in China from 2010 to 2017

3.3 United States

3.3.1 Carbon emissions

From 2010 though 2017, the overall fossil fuel CO₂ emissions in the United States showed a downward trend. In 2010 and 2014, emissions peaked at 1.50 and 1.46 Pg C/yr respectively. The lowest CO₂ emissions were 1.39 Pg C/yr in 2017 (Fig. 3–8).

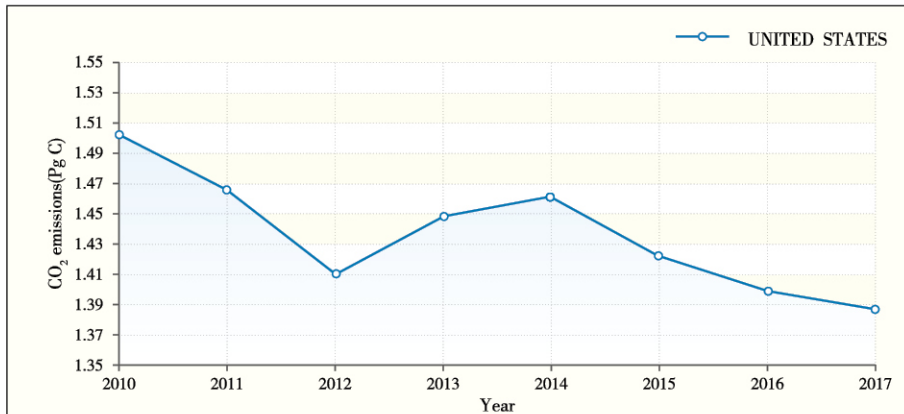


Fig. 3–8 US fossil fuel CO₂ emissions from 2010–2017, data based on BP (<https://www.bp.com/content/dam/bp/en/corporate/excel/energy-economics/statistical-review/bp-stats-review-2018-all-data.xlsx>)

Note: The CO₂ emissions data based on BP reflect only those through consumption of oil, gas and coal for combustion related activities

3.3.2 Industrial adjustment contributions to carbon emissions reduction

Compared with thermal power, the carbon emissions reduction from hydroelectricity, wind, solar and nuclear generation has increased each year from 2010 to 2017 (Fig. 3–9). In 2017, the total carbon emission reduction of hydroelectricity, wind, solar and nuclear was 348.57 Tg C.

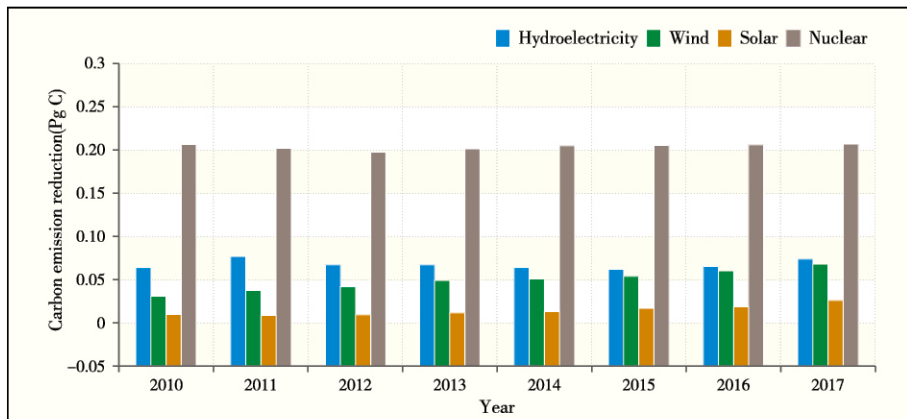


Fig. 3–9 Carbon emissions reduction introduced by hydroelectricity, wind, solar and nuclear use in 2010–2017. Power generation data based on BP (<https://www.bp.com/content/dam/bp/en/corporate/excel/energy-economics/statistical-review/bp-stats-review-2018-all-data.xlsx>)

3.3.3 Terrestrial ecosystem carbon sink

Based on the ecosystem model, the North American carbon sinks from 2000 to 2009 are about 0.3–0.9 Pg C/yr, and the multi-year average is about 0.5 Pg C/yr. In the past 30 years (1980–2010), US terrestrial ecosystems have been carbon sinks and increased at a rate of 0.09 Pg C/year, which is about 30% of North American fossil fuel emissions.

The analysis of the NDVI dataset shows that the annually averaged NDVI increases significantly in the United States during the years 2010 through 2017, with a linear regression slope of 0.0038/yr (Fig. 3–10). In terms of spatial distribution, the area for significant improvement in NDVI accounted for 15.6% of the national land area, mainly in the northeastern, central, and western regions. The percentage of area that saw significant reduction in NDVI was only 1.0%, mainly in the western coastal areas and Northwestern United States.

These changes indicate an increasing trend in carbon sequestration of terrestrial ecosystems in the United States (Fig. 3–11).

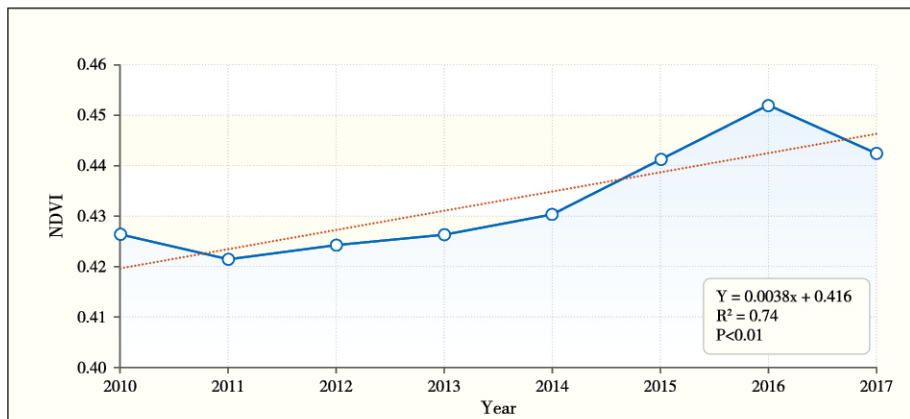


Fig. 3–10 Interannual variation of the annual mean NDVI in the United States from 2010 to 2017. The blue hollow dots indicate the annual mean of NDVI, and the red line indicates the NDVI trend line for 2010–2017

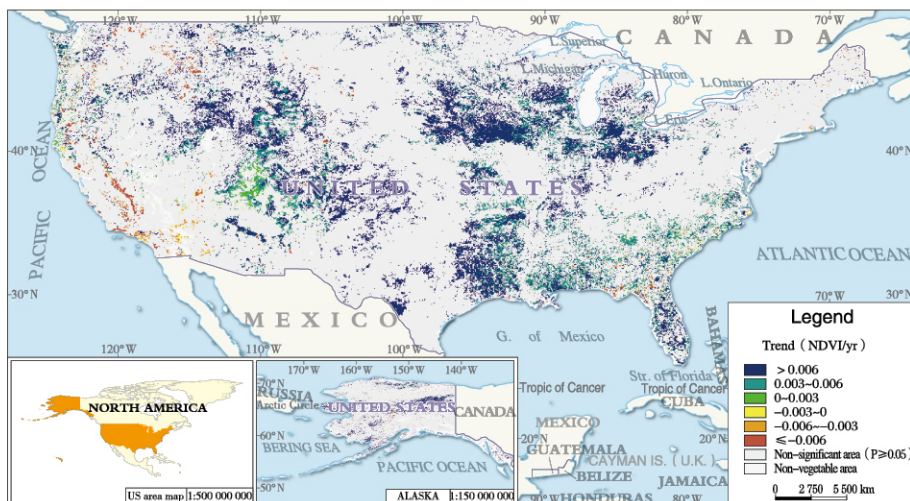


Fig. 3–11 Mean annual NDVI trend and spatial significance test in the United States from 2010 to 2017

3.4 Major countries in Europe

3.4.1 Carbon emissions

From 2010 through 2017, the overall fossil fuel CO₂ emissions in France showed a downward trend. In 2010, CO₂ emissions were 0.10 Pg C, and fell in 2017 to 0.09 Pg C. Germany's CO₂ emissions are relatively stable during this period. The downward trend of CO₂ emissions in the UK is more obvious. In 2010, CO₂ emissions were 0.14 Pg C, and fell in 2017 to 0.11 Pg C. In general, CO₂ emissions in major European countries are slowly declining (Fig. 3-12).

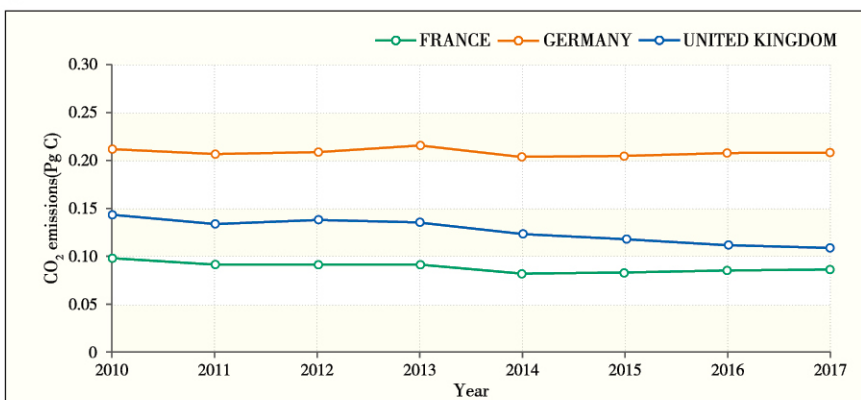


Fig. 3-12 Major European countries fossil fuel CO₂ emissions from 2010–2017, data based on BP (<https://www.bp.com/content/dam/bp/en/corporate/excel/energy-economics/statistical-review/bp-stats-review-2018-all-data.xlsx>)

Note: The CO₂ emissions data based on BP reflect only those through consumption of oil, gas and coal for combustion related activities.

3.4.2 Industrial adjustment contributions to carbon emissions reduction

From 2010 through 2017, compared with thermal power, the carbon emission reduction from hydroelectricity, wind, solar and nuclear generation has increased yearly. In 2017, the total carbon emission reduction in France,

Germany, and the UK of hydroelectricity, wind, solar and nuclear were 114.36, 57.26, 32.75 Tg C, respectively (Fig. 3–13, Fig. 3–14, and Fig. 3–15).

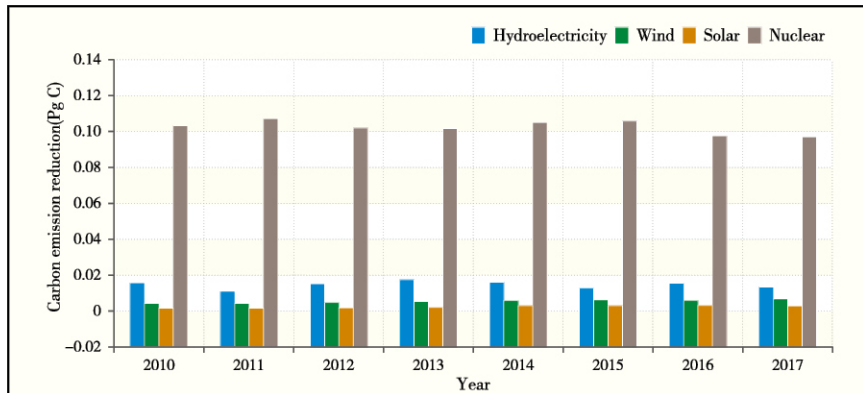


Fig. 3–13 Carbon emissions reduction introduced by hydroelectricity, wind, solar and nuclear use in 2010–2017 in France. Power generation data based on BP (<https://www.bp.com/content/dam/bp/en/corporate/excel/energy-economics/statistical-review/bp-stats-review-2018-all-data.xlsx>)

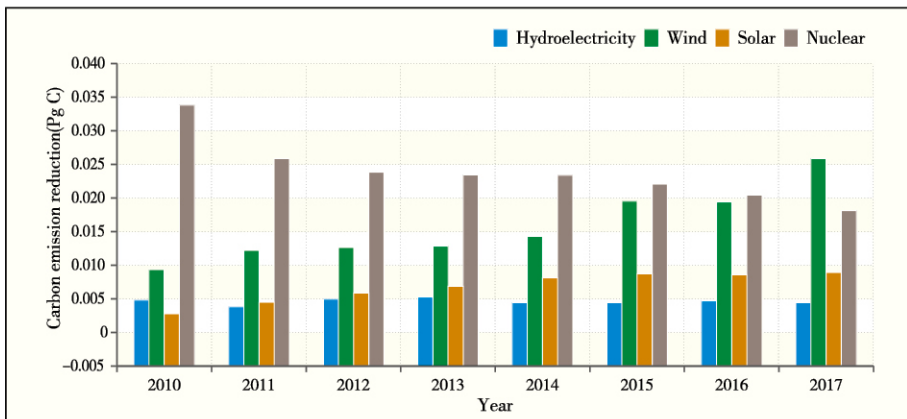


Fig. 3–14 Carbon emissions reduction introduced by hydroelectricity, wind, solar and nuclear use from 2010–2017 in Germany. Power generation data based on BP (<https://www.bp.com/content/dam/bp/en/corporate/excel/energy-economics/statistical-review/bp-stats-review-2018-all-data.xlsx>)

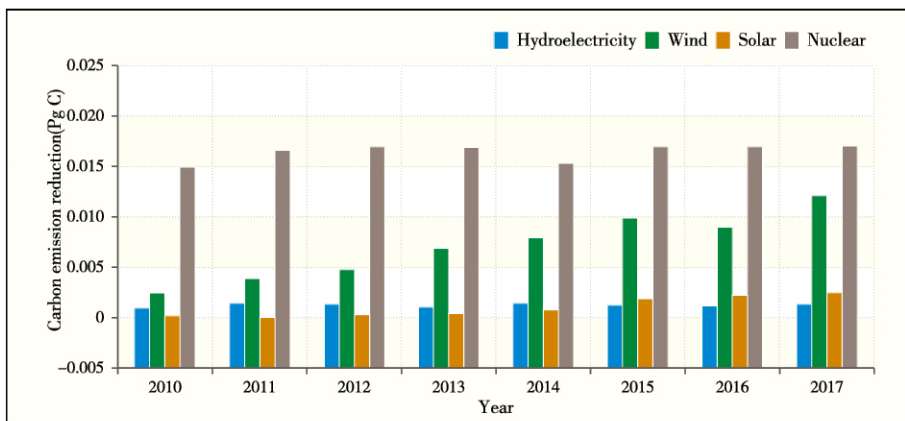


Fig. 3–15 Carbon emissions reduction introduced by hydroelectricity, wind, solar and nuclear use from 2010–2017 in UK. Power generation data based on BP (<https://www.bp.com/content/dam/bp/en/corporate/excel/energy-economics/statistical-review/bp-stats-review-2018-all-data.xlsx>)

3.4.3 Terrestrial ecosystem carbon sinks

The European terrestrial ecosystem is an important carbon sink with a magnitude of approximately 0.08–0.60 Pg C/yr and an average carbon sink of approximately 0.3 Pg C/yr. Among them, the carbon sink of the European forest ecosystem is about 0.4 Pg C/yr, and the carbon sink of the grassland ecosystem is about 0.1 Pg C/yr. The European terrestrial ecosystem carbon sink can offset about 7–12% of European anthropogenic carbon emissions in 1995.

The analysis of NDVI data for Europe shows that the annually averaged NDVI in Europe increased from 2010 to 2017, but the trend is not significant (Fig. 3–16). Looking at the spatial distribution of NDVI, the area for significant improvement in NDVI accounted for 10.1% of the Europe land area (at the significant level of 0.05), mainly in the countries of Germany, Poland, and the United Kingdom. The percentage of area that shows significant reduction in

NDVI was only 1.1%. This change also confirmed the trend of non-significant growth of carbon sinks in European terrestrial ecosystems (Fig. 3–17).

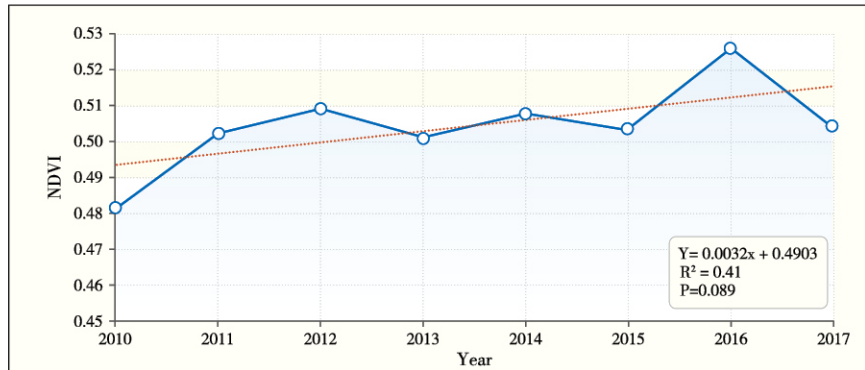


Fig. 3–16 Interannual variation of mean annual NDVI in Europe from 2010 to 2017. The blue hollow dots indicate the annual mean of NDVI, and the red line indicates the NDVI trend line from 2010–2017



Fig. 3–17 Mean annual NDVI trend and spatial significance test in Europe from 2010 to 2017

References

- Boden T, Marland G, Andres R. Global, regional, and national fossil-fuel CO₂ emissions. Oak Ridge National Laboratory, U.S. Department of Energy, Oak Ridge, Tenn., U.S.A., doi 10.3334/CDIAC/00001_V2017, 2017; available at: http://cdiac.ess-dive.lbl.gov/trends/emis/overview_2014.html
- BP. <https://www.bp.com>
- China Electricity Council. <http://www.cec.org.cn/guihuayutongji/tongjinxini/>
- Du S, Liu L, Liu X, et al. Retrieval of global terrestrial solar-induced chlorophyll fluorescence from TanSat satellite, Science Bulletin (2018), doi: <https://doi.org/10.1016/j.scib.2018.10.003>
- Duveiller G, Cescatti A. Spatially downscaling sun-induced chlorophyll fluorescence leads to an improved temporal correlation with gross primary productivity. Remote Sensing of Environment, 2016, 182,72–89.
- Fang K, Zhu X, Gao K, et al. Carbon footprint of global electricity and its equivalent calculation. Chinese Journal of Ecology, 2012,31(12) : 3160–3166.
- Fang J, Guo, Z, Piao S, et al. Terrestrial vegetation carbon sinks in China, 1981–2000. Science in China Series D: Earth Sciences, 2007,(06):804–812.
- FLUXNET2015. <http://fluxnet.fluxdata.org/data/fluxnet2015-dataset/>
- International Energy Agency. CO₂ emissions from fuel combustion highlights (2017 edition) .
- Jang Y. Water–Carbon footprint accounting and scenario simulation study of China's regions and industrial sectors. Tsinghua University,2015.
- Le Quéré C, Andrew R, Friedlingstein P, et al. Global Carbon Budget 2017. Earth System Science Data, 2018(10),405–448.

Liu H. Study on carbon emissions allocation of final energy consumption in China. Jilin University, 2013.

Liu Y, Kalnay E, Zeng N, et al. Estimating surface carbon fluxes based on a local ensemble transform kalman filter with a short assimilation window and a long observation window. Geoscientific Model Development, <https://doi.org/10.5194/gmd-2017-269>.

Liu Y, Wang J, Yao L, et al. The TanSat mission: preliminary global observations. Science Bulletin, 2018, 63(18):1200–1207.

Ma Z. Comparative evaluation of greenhouse gas emission coefficients of several major energy sources in China. China Institute of Atomic Energy, 2002.

NASA. <http://a://avdc.gsfc.nasa.gov/>

Oda T, Maksyutov S, Andres R. The Open-source Data Inventory for Anthropogenic CO₂, version 2016 (ODIAC2016): a global monthly fossil fuel CO₂ gridded emissions data product for tracer transport simulations and surface flux inversions. Earth System Science Data, 10, 87–107, <https://doi.org/10.5194/essd-10-87-2018>, 2018.

Peters W, Jacobson A,et al. An atmospheric perspective on North American carbon dioxide exchange: CarbonTracker. Proceedings of the National Academy of Sciences U S A, 2007, 104, 18925–18930.

Qin D. Developing hydropower can effectively reduce carbon dioxide emissions. Sichuan Water Power,2011,30(02):71–75+78.

Shi X, Li X, Yang J. Research on carbon reduction potential of electric vehicles for low-carbon transportation and its influencing factors. Environmental Science, 2013,34(01):385–394.

Tang X, Zhao X, Bai Y, et al. Carbon pools in China's terrestrial ecosystems: New estimates based on an intensive field survey. *Proceedings of the National Academy of Sciences*, 2018a, 115(16), 4021–4026.

Wang J, Zeng N, Wang M, et al. Contrasting terrestrial carbon cycle responses to the 1997/98 and 2015/16 extreme El Niño events. *Earth System Dynamics*, 2018, 9, 1–14.

Xia D. The research on life cycle carbon emissions measurement of electric power generation side based on the scenario analysis method. Chongqing University, 2010.

Yang D, Liu Y, Cai Z, et al. First global carbon dioxide maps produced from TanSat measurements. *Advances in Atmospheric Sciences*, 2018, 35(6), 621–623.

Zeng N, Mariotti A, Wetzel P. Terrestrial mechanisms of interannual CO₂ variability. *Global Biogeochemical Cycles*, 2005, 19, GB1016, 10.1029/2004gb002273.

Zeng N, Zhao F, Collatz G, et al. The agricultural Green Revolution as a driver of the increasing atmospheric CO₂ seasonal amplitude. *Nature*, 2014, 515(7527), 394–397.

Zhao M. Structural changes and driving mechanism of carbon sources and sinks in Shanghai. East China Normal University, 2010.

Edited by:

Institute of Atmospheric Physics, Chinese Academy of Sciences

Institute of Geographic Sciences and Natural Resources Research,
Chinese Academy of Sciences

Institute of Remote Sensing and Digital Earth, Chinese Academy of
Sciences

National Satellite Meteorological Center

Nanjing University

Chinese Academy for Environmental Planning

Department of Atmospheric and Oceanic Science and Earth System
Science, Interdisciplinary Center, University of Maryland

Universities Space Research Association



National Remote Sensing Center of China,
Ministry of Science and Technology of the People's Republic of China

Address: Beijing City, South Lane Haidian District Liulin No. 8 Building West Pavilion

Tel: (010)58881180

Fax : (010)58881179

E-mail: geoarc@nrsc.gov.cn

Web: www.nrsc.gov.cn